Bioinspired stability enhancement in deuterium-substituted organic-inorganic hybrid perovskite solar cells

Jinhui Tong,[1†] Xun Li,[2†] Jianxin Wang,[2] Haiying He,[3*] Tao Xu,[2*] Kai Zhu[1*]

[1]Chemistry and Nanoscience Center, National Renewable Energy Laboratory, Golden, Colorado 80401, USA

[2]Department of Chemistry and Biochemistry, Northern Illinois University, DeKalb, Illinois 60115, USA

[3]Department of Physics and Astronomy, Valparaiso University, Valparaiso, Indiana 46383, USA

[*]Corresponding authors: Kai.Zhu@nrel.gov (K.Z.); txu@niu.edu (T.X.); haiying.he@valpo.edu (H.H.)

[†]These authors contributed equally to this work.

Abstract

In hybrid perovskite solar cells (PSCs), the reaction of hydrogens (H) located in the amino group of the organic A-site cations with their neighboring halides plays a central role in degradation. Inspired by the retarded biological activities of cells in heavy water, we replaced the light H atom with its abundant, twice-as-heavy, nonradioactive isotope, deuterium (D) to hamper the motion of H. This D substitution retarded the formation kinetics of the detrimental H halides in Pb-based PSCs, as well as the hydrogen-bond mediated oxidation of Sn^{2+} in Sn-Pb-based narrow bandgap PSCs, evidenced by accelerated stability studies. A computational study indicated that the zero point energy of D-based formamidinium (FA) is lower than that of pristine FA. In addition, the smaller increase in entropy in D-based FA than in pristine FA accounts for the increased formation free energy of the Sn^{2+} vacancies, which leads to the retarded oxidation kinetics of Sn^{2+}. In this study, we show that substituting active H with D in organic cations is an effective way to enhance the stability of PSCs without sacrificing photovoltaic (PV) performance. This approach is also adaptable to other stabilizing methods.

Significance statement

The slow motion of deuterium (D) in amino group of A-site cations of hybrid perovskite impedes the detrimental formation of hydrogen halides, thus retards the degradation kinetics of hybrid perovskite. D substitution also improve the stability of narrow bandgap perovskites by impeding the hydrogen-bond mediated Sn^{2+} oxidation to Sn^{4+}, rendering a retrofit adaptable to all other existing stabilizing methods for hybrid perovskites and inspiring an alternative way to slow down a variety of materials degradation kinetics relevant to hydrogen mobility.

Keywords: deuterium, hybrid perovskite, stability, solar cells, degradation, kinetics

Introduction

The certified champion power conversion efficiency (PCE) of perovskite solar cells (PSCs) is currently on par with or greater than that of silicon (Si)- and copper indium gallium selenide (CIGS)-based solar cells. In addition, solution processing makes PSCs a low-cost photovoltaic (PV) technology. However, there are still major challenges in achieving future widespread market adoption of PSCs, particularly their limited long-term stability. PSCs suffer from ~5%–10% PCE degradation over a few thousand hours under continuous operation.[1-3] In contrast, Si-based solar cells exhibit a >20-year lifetime warranty with an average PCE degradation rate of only 0.5% per year.

The general chemical formula of metal halide perovskites is ABX_3, where A is a monovalent mono, double, or triple cation—including organic $CH_3NH_3^+$ (MA^+) and $CH(NH_2)_2^+$ (FA^+) and/or inorganic Cs^+, Rb^+, and K^+. The A-site cations of state-of-the-art Pb-based PSCs typically use organic cations with N-H and C-N bonds. The rotating and stretching modes of these bonds have essential contributions to the high dielectric response and the high stability of excitons that retard the recombination rate through reorientation of organic cations.[4–7] Explicitly, the rotating and stretching modes of the polar C-N and N-H bonds of the organic cations inside the inorganic PbX_6^- cages deform and agitate, stabilizing the photoexcited inorganic framework through their electrostatic interactions with the inorganic lattice.[4, 7] However, the polar N-H bond is the most vulnerable bond in hybrid perovskites under stress factors (e.g., potential, moisture, radiation, heat, and oxygen).[8–15] Polar N-H bonds split easily because the H atom is the lightest atom and can readily migrate to trigger a series of unwanted degradation reactions that lead to instability of PSCs, including the formation of HO_2 with O_2 [16–18] and/or H-I.[19–21] The former proceeds to form $Pb(OH)_2$ and PbO with Pb, and the latter disintegrates to H_2 and I_2, which can

readily escape from the reaction center via defects in the film, further pushing the equilibrium toward degradation.

The stability issue becomes even more prominent in high-efficiency all-perovskite tandem solar cells because of the use of Sn-Pb mixed perovskite materials. Sn-Pb narrow-bandgap PSCs has achieved PCEs exceeding 20%.[22] However, due to the strong inert pair effect in Sn^{2+} relative to Pb^{2+}, the oxidation potential of $Sn^{2+} \rightarrow Sn^{4+} + 2e^-$ (+0.15 V) is much lower than that of $Pb^{2+} \rightarrow Pb^{4+} + 2e^-$ (+1.67 V). The unavoidable oxidation of Sn^{2+} to Sn^{4+} is a primary cause of the poor long-term stability of Sn-containing PSCs.[23–25] The oxidation of Sn^{2+} to Sn^{4+} is relevant to the formation of hydrogen bonds between organic A-site cations and ingress H_2O molecules and to the impact of A-site cation-induced polarization on the defect formation energy that regulates the emergence of Sn^{2+} from bulk to surface. Specifically, the organic cation in perovskites can adsorb H_2O via the hydrogen bonds between the N (or H) from organic cations and the H (or O) from H_2O.[26] The stronger hydrogen bond of N···H can more tightly lock H_2O with the A-site cation so as to slow down H_2O-mediated oxidation of Sn^{2+} to Sn^{4+}; the weaker hydrogen bond of H···O, however, allows relatively faster H_2O-mediated migration of O_2 to the deep lattice, thus faster oxidation of Sn^{2+} to Sn^{4+}.[26–28] In parallel, the oxidation of a surface Sn^{2+} by O_2 generates a Sn^{2+} vacancy due to the migration of the resulting SnO_2.[29, 30] As a result, the inward polarization (due to vibration and/or rotation of polar bonds such as N-H) of A-site cations leads to a downhill slope of defect formation energy for Sn^{2+} vacancies from surface to subsurface layers, causing Sn^{2+} to emerge from subsurface layers to the surface.[29–34] It is thus evident that the unwanted motion of H is a notable root cause of the instability in PSCs containing organic A-site cations and Sn^{2+}.

Inspired by the emerging longevity aging study in biological science, particularly the slow growth of yeast cells in heavy water,[35] we herein report a nuclear approach to retard any H-

dependent degradation reactions in both Pb-based and Sn-Pb-based PSCs by replacing H with its heavier but nonradioactive and resourceful isotope deuterium (D). Because D is twice as heavy as H, the kinetics of all the degradation mechanisms related to the motion of H can be substantively slowed down, leading to a marked enhancement in device stability in accelerated aging tests. In particular, the replacement of H by D can notably attenuate the frequency of the hydrogen bonds by a factor of $(2)^{1/2}$ and lower the zero point vibrational energy in the hydrogen bonds.[27] The smaller dipole moment and slightly shorter bond length of D-N compared to H-N [32, 33] retards the polarization of the neighboring inorganic framework—namely the emergence of Sn^{2+} from the subsurface to the surface by A-site organic cations—so as to reduce the oxidation of Sn-containing perovskites. Note that the replacement of N-H with N-D can be conveniently achieved by soaking and recrystallizing the organic precursors (e.g., methylammonium iodide [MAI] and formamidinium iodide [FAI]) in D_2O). Ocean water provides a source of D that is more than sufficient to supply the needs of any future PSC-based PV applications (see technoecono analysis of D-based perovskite in supplementary materials, **Note S1**).

Results and Discussion

We first study the inertness of D-substituted FA and MA using the Tyndall effect, which is a direct, visual method for distinguishing the stabilities of H-based organic cations from those of D-based organic cations. We prepared two perovskite precursory solutions for comparison, including an H-based solution containing methylammonium iodide (MAI or CH_3NH_3I), butylamine (BA or $CH_3(CH_2)_3NH_2$), and PbI_2; and a D-based precursory solution containing deuterated methylammonium iodide (D-MAI or CD_3ND_3I), BA, and PbI_2. Both solutions have a molar ratio of 1:1:1 for the three ingredients at a concentration of 200 mg/mL with reference to

PbI_2. **Figure S1** shows that initially, both solutions appeared homogeneous and no Tyndall effect was observed. However, after the solutions were aged on a hot plate at 55°C for 8 days, precipitates formed in the D-$MAPbI_3$ precursor solution, clearly visualized by the Tyndall effect. The Tyndall effect was observed only in the precursor solution containing $CD_3ND_3PbI_3$. The reaction mechanism is outlined below, with the downward arrow used to indicate the precipitation.

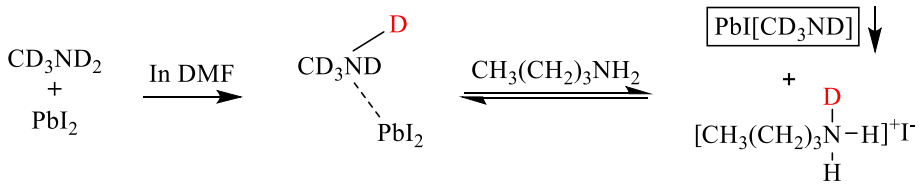

(1)

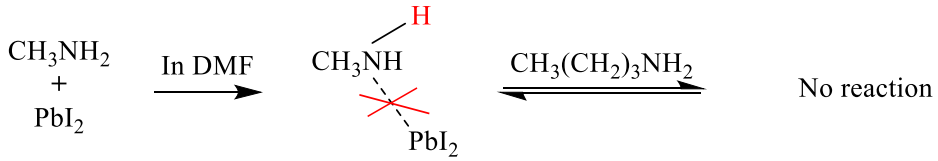

(2)

In reaction (1), due to the low acidity of the D-based MA (owing to the retarded motion of D), the D-based MA behaves as a base and forms a complex with PbI_2 through a Lewis acid-base reaction (the Pb^{2+} cation is the Lewis acid, and the lone pair of electrons on the N of the D-based MA is the Lewis base). This reaction outpaces the reaction between the Lewis acid Pb^{2+} and the Lewis base dimethylformamide (DMF) molecules. The resulting complex ($CD_3ND_2\cdots PbI_2$) is acidic enough (N-D is activated) to be deprotonated by a strong base of butylamine (donor number = 42 kcal/mol). However, it cannot be deprotonated by DMF, because DMF (donor number = 26 kcal/mol) is a weaker base than butylamine. Finally, a precipitate of D-PbI-methylamide iodide (the conjugated base of the $CD_3ND_2\cdots PbI_2$ complex) and a salt of D-butylammonium iodide (the conjugate acid of butylamine) is generated.[36] In the case of reaction (2), due to the faster motion

of H than D, and possibly the lower dissociation energy of N-H than N-D,[37] the H-based MA exhibits higher acidity than D-based MA or DMF molecules—in other words, H-based MA is a weaker base than D-based MA or DMF. Thus, the Lewis acid Pb^{2+} preferentially reacts with the lone pair of electrons on O of the DMF molecules (a Lewis base), instead of reacting with the weaker Lewis base of the H-based MA. As a result, there is no subsequent intermediate complex formed because of the complete solvation of Pb^{2+} by DMF molecules.

We further assessed the antioxidation property between H-based perovskite and D-based perovskite films by exposing the perovskite films to highly energetic oxygen plasma for accelerated oxidation. Two different perovskite compositions were used: $(CH(NH_2)_2SnI_3)_{0.6}(CH_3NH_3PbI_3)_{0.4}$ (denoted as "H-based"), and $(CH(ND_2)_2SnI_3)_{0.6}(CD_3ND_3PbI_3)_{0.4}$ (denoted as "D-based"). Fourier transform infrared spectroscopy (FTIR) was used to characterize the change of functional groups in the perovskite thin films before and after oxygen plasma treatment. With increasing oxygen plasma treatment time, FTIR of the H-based perovskite film (**Figure 1(a)**) showed attenuated intensities for peaks at $\nu \approx 3402$ cm^{-1} (N-H stretching), $\nu \approx 3271$ cm^{-1} (C-H stretching), $\nu \approx 1712$ cm^{-1} (C=N stretching, characteristic to FA), $\nu \approx 1612$ cm^{-1} (N-H bending), and $\nu \approx 1470/1350$ cm^{-1} (C-H bending). These results indicate the oxidation of these functional groups, namely, the insertion of oxygen atoms, which is further evidenced by the corresponding growth of two new peaks at $\nu \approx 3749$ cm^{-1} (free O-H stretching) and $\nu \approx 1519$ cm^{-1} (N-O stretching) with increasing oxygen plasma treatment time. After 100 s of oxygen plasma treatment, only the O-H stretching, N-O stretching, and part of C=N stretching bonds could be detected. In a remarkable contrast, almost no changes were observed in the FTIR of the D-based samples, as shown in **Figure 1(b)**, even after 100 s of oxygen plasma treatment. This comparison indicates that the N-D or C-D bonds are more inert than N-H

155 or C-H bonds, due to the comparative heaviness of D, which impedes its motion and therefore its
156 ability to accommodate the oxygen insertion.

157 To experimentally evaluate the effect of D-substituted organic A-site cations on the PV
158 performance of PSCs, we first studied pure Pb-based perovskites with the composition of
159 $Cs_{0.05}MA_{0.15}FA_{0.8}PbI_{2.55}Br_{0.45}$ using a standard p-i-n configuration (indium tin oxide (ITO)/
160 poly(triaryl amine) (PTAA)/perovskite/C_{60}/bathocuproine (BCP)/Ag). **Figure 2(a)** shows the
161 comparable current density-voltage (J-V) curves from the H-based devices (both MA and FA are
162 pristine H-based) and the D-based devices (both MA and FA are D-based). Note that neither type
163 of device was encapsulated. Both H-based and D-based devices exhibited nearly the same J-V
164 behaviors, with no observable hysteresis, indicating that deuteriation does not affect the PV
165 performance of the devices. **Figure 2(b)** shows the device stability after thermal aging at 85ºC for
166 150 h in dry air. Strikingly, the D-based devices retain most of their initial PCE, whereas the
167 pristine H-based devices exhibit less than 40% of their initial PCE.

168 To gain mechanistic insight into the enhanced thermal stability of D-based devices, we
169 further calculated the vibrational frequencies of the N-H and N-D bonds in the H-based and D-
170 based FA (see **Table S1 and Fig. S2**). The calculated N-H frequencies are in the range of 3415–
171 3537 cm^{-1}, in good agreement with the experiment. In contrast, the N-D frequencies are a factor
172 of just 0.723–0.742 of the N-H ones, indicating that N-D vibration is drastically retarded.
173 Therefore, the reaction kinetics involving the motion of H can be largely slowed down by replacing
174 H with D, in good agreement with our experimental study. The calculated zero point energy (ZPE)
175 of D-based FA is lowered by 0.36 eV (i.e., 4123 K) relative to that of H-based FA. Because the
176 electronic properties do not change with the substitution of H by D, the enhanced thermal stability

of D-based PSCs can be logically attributed to the slow motion of D, which retards the kinetics of the degradation reactions.

Sn doping of perovskites enables promising narrow-bandgap PSCs (denoted Sn-Pb PSCs) for enhanced current density. To study the impact of D-substituted organic A-site cations on Sn-doped perovskites, we chose the MA-free perovskite composition of $Cs_{0.25}FA_{0.75}Sn_{0.5}Pb_{0.5}I_3$ to avoid complications from the deleterious effect of MA^+ volatility. **Fig. S3** shows the X-ray diffraction (XRD) patterns of $Cs_{0.25}FA_{0.75}Sn_{0.5}Pb_{0.5}I_3$ using H-FAI (H-based) and D-FAI (D-based) as the organic A-site cation, respectively. The XRD patterns of both the H-based film and the D-based film show identical features in terms of peak position, peak intensity, and peak width, indicating that deuterium substitution does not change film lattice structure and crystallinity. We also conducted scanning electron microscopy (SEM) to compare the film morphology, as shown in **Fig. S4**. This figure shows that both films exhibit similar representative grain size and film morphology. Thus, deuterium substitution does not affect film morphology either.

Figure 3(a) compares the J-V curves of the narrow-bandgap PSCs based on $Cs_{0.25}FA_{0.75}Sn_{0.5}Pb_{0.5}I_3$ with H-FAI and D-FAI as the organic A-site cations. Note that these narrow-bandgap PSCs were made under the same conditions and were not encapsulated. When measured under a reverse voltage scan, the narrow-bandgap PSC made with H-FAI exhibited a PCE of 20.845% with a short-circuit current density (J_{sc}) of 31.271 mA cm^{-2}, an open-circuit voltage (V_{oc}) of 0.825 V, and a fill factor (FF) of 0.808. When measured under a forward voltage scan, the H-FAI-based narrow-bandgap PSC showed a PCE of 20.682% with a J_{sc} of 31.218 mA cm^{-2}, a V_{oc} of 0.823 V, and an FF of 0.805. D-based devices show similar J-V performance to that of H-based devices, exhibiting a PCE of 20.371% for reverse scan and 20.335% for forward scan. **Figure 3(b)** compares the stabilized power output (SPO) efficiencies. H-based devices have an

SPO efficiency of 20.750%, very close to the SPO efficiency of 20.158% for D-based devices. It is clear that both H-based and D-based narrow-bandgap PSCs show similar PV performance, indicating that the substitution of D for H does not affect the normal PV performance.

We further conducted an accelerated evaluation on the operational stability of the encapsulated narrow-bandgap PSCs in air with a relative humidity (RH) of ~50% and a temperature of ~50°C under continuous light illumination in air. Both H-based and D-based narrow-bandgap PSCs were biased near the maximum power point during illumination. As can be seen in **Figure 3(c)**, the H-based Sn-Pb PSC showed about 29.3% efficiency loss after 550 h of illumination, whereas the D-based Sn-Pb PSC showed markedly enhanced stability, with only 11.4% degradation. We further tested the stability of unencapsulated H-based and D-based Sn-Pb narrow-bandgap PSCs in air (~80% RH). As shown in **Figure 3(d)**, the D-based Sn-Pb PSC showed notably better atmospheric stability than the H-based Sn-Pb PSC. The D-based Sn-Pb PSC retained 82% of its initial efficiency after 8 h of storage in humid air, whereas the H-FAI based device retained only of 71% of its initial efficiency during the same period.

We also conducted computational modeling and simulation based on density functional theory (DFT) to provide a fundamental understanding of the remarkably enhanced antioxidation of Sn^{2+} to Sn^{4+} found in the D-based narrow-bandgap PSCs under humid conditions in open air. First, we constructed an FA···H_2O complex model in order to investigate the impact of deuteration of the N-H bond in FA on the diffusion of H_2O molecules into the bulk. In the equilibrium state, an H bond is formed as N-H···O (**Fig. S5**), which results in an H_2O binding energy of 0.65 eV and an elongation of the N-H bond from 1.01 to 1.03 Å. Consequently, the vibrational frequency of the N-H stretching mode is reduced by a factor of ~0.9 (**Table S2** and **Fig. S6**). Substituting D for

H further reduced the vibrational frequencies by a factor of ~0.7, which in turn, slowed down the diffusion of water molecules.

The oxidation of Sn^{2+} into Sn^{4+} (i.e., SnO_2) is most likely to start from the surface of the perovskite as it is exposed to water and oxygen in humid air. Earlier studies have shown that, regardless of the A-site cation in a hybrid $ASnX_3$ perovskite, the reaction between Sn^{2+} and adsorbed O_2 is energetically favorable, which leads to the formation of SnO_2 and Sn^{2+} vacancies (V_{Sn}^{2-}) at the outermost surface.[30] The Sn^{2+} ions underneath may migrate to fill in the Sn^{2+} vacancies and form vacancies below. As this process continues, more Sn^{2+} ions propagate to the surface and get oxidized to Sn^{4+}, while the Sn^{2+} vacancies move down into the bulk. Consequently, $ASnX_3$ degrades to A_2SnX_6, destroying the PSC performance. Additionally, the study of $MASnBr_3$ has demonstrated that the polarization induced by MA ions at the A-site with a specific orientation can significantly expedite the migration of V_{Sn}^{2-} from the surface to the bulk region compared to the nonpolar Cs ions.[30] We employed a model system of the $FASn_{0.5}Pb_{0.5}I_3$ (001) surface to investigate the dependence of the defect formation energy of V_{Sn}^{2-} on its location, the Sn chemical potential μ(Sn), and the deuteration effect. To study the dependence of the vacancy formation energy on the location of the vacancy underneath the surface, we generated the Sn vacancy in the first, second, and third layers of the (001) surface. It is interesting to note that the orientation of FA cations tilted near the Sn vacancy (**Fig. S7**). To reveal the deuteration effect by substituting D for H in the FA molecule, we calculated the vibrational frequencies of the system, thereby obtaining the free energy corrections (at T = 298.15 K) to the formation energy of V_{Sn}^{2-} (see **Table S3**). The calculated formation free energies (ΔG_f) of V_{Sn}^{2-} at different depths (layers) beneath the top surface layer are plotted as a function of μ(Sn) in **Figure 4**. The canted lines indicate the change of formation energies as μ(Sn) increases from the equivalent chemical potential of Sn in the SnO_2 bulk (O_2-rich)

to that of a Sn-rich environment. Note that the positive formation energy indicates that the formation of a vacancy requires energy, whereas the negative formation energy at lower μ(Sn) suggests a spontaneous process.

These results show a similar trend as the previous study,[30] where at a certain μ(Sn), ΔG_f decreases with the increase in depth of the Sn vacancy location, along the same direction as the polarization caused by the FA cations. However, the difference in the value of ΔG_f is smaller than in the case of $MASnBr_3$. This is likely due to the fact that the FA cation has a much smaller intrinsic dipole moment (0.081 Debye) than the MA cation (0.845 Debye), in agreement with the observed better stability of FA. In addition, the deuteration of FA increases the formation free energy of V_{Sn}^{2-} by 0.76 eV, largely due to the smaller increase in entropy in the defective system with V_{Sn}^{2-} than in the pristine surface without vacancies (see **Table S3**). These results reveal that the adoption of a deuterium-substituted organic component reduces the degree of oxidation of the Sn^{2+} cations.

In summary, the replacement of H—particularly the active H in the amino group—with D is an effective approach to reducing the vibration frequency of the N-D bond that is accountable for the degradation kinetics of perovskites under stress factors such as heat and light. The deuteration of organic cations also reduced the entropy change in D-FA. This helped increase the formation free energy of the Sn^{2+} vacancies, impeding the emergence of Sn^{2+} to the surface layer where oxidation occurs. Thus, it is evident that substitution of active H with D in organic cations is a standalone kinetic method to enhance the stability of PSCs, as well as a conveniently adaptable retrofit to any other stabilizing methods that does not require changing procedures or compositional formula.

Materials and Methods

1. Synthesis of deuterium-replaced FAI and MAI

Synthesis of deuterated $CH(ND_2)_2I$ (D-FAI). $CH(NH_2)_2I$ (FAI, Greatcell Solar Materials Pty Ltd.) was dissolved in excessive deuterium oxide (Sigma-Aldrich, 99.9 atom %) at a molar ratio of 1:40 under stirring, followed by heating the solution to 90°C for 2 hours under argon (Ar). The liquid was then evaporated at 70°C under a flow of Ar to dry off. This process was repeated three times to ensure complete substitution of ammonium hydrogen by deuterium to yield the high purity of D-FAI. Finally, the white solid was collected and moved to the vacuum oven at 60°C overnight for further drying. In principle, most of the D_2O can be recollected by reflux for future scaled-up synthesis.

Synthesis of deuterated CD_3ND_3I (D-MAI). First, CD_3NH_2 gas (Sigma-Aldrich, 99.9 atom %) was slowly reacted with an equimolar amount of hydroiodic acid (HI) solution (Sigma-Aldrich, 57 wt% in water) in a round-bottom flask soaked in an ice bath. Then, the solvent of this solution was dried off by rotary evaporation at 60°C. The collected solid of CD_3NH_3I with HI residual was further washed by anhydrous ethyl ether (Fisher Chemical) under vacuum filtration, followed by drying the white solid in the vacuum oven at 60°C overnight. Next, the collected CD_3NH_3I was dissolved in excessive deuterium oxide at a molar ratio of 1:40 with stirring, followed by heating the solution to 90°C for 2 hours under Ar and then evaporating the solution at 70°C under flowing Ar to dry off the solvent. This process was repeated three times to ensure complete substitution of N-H by N-D to yield the high purity of D-MAI. Finally, the white solid was collected and transferred to the vacuum oven at 60°C overnight for further drying. All samples were characterized by nuclear magnetic resonance (NMR) spectroscopy, performed using a Bruker Spectrospin 500-MHz NMR spectrometer. **Figs. S8**, **S9**, and **S10** show the NMR results of

$CH(NH_2)_2I$, $CH(ND_2)_2I$, and the solvent (deuterated dimethyl sulfoxide [DMSO]) used in the NMR study, respectively. NMR results for CH_3NH_3I and CD_3ND_3I were reported in our previous work.[38]

2. Oxygen-plasma oxidation of perovskite films

The accelerated oxidation of different perovskite films was conducted using a plasma cleaner (PDC-32G, Harrick Plasma). This plasma cleaner includes three gears: low energy, medium energy, and high energy.

3. Preparation of perovskite solar cell precursor

All the perovskite solution and film depositions were conducted in a N_2 glovebox with O_2 level < 1 ppm and H_2O < 1 ppm. For the H-based Pb-Sn mixed narrow bandgap $Cs_{0.25}FA_{0.75}Sn_{0.5}Pb_{0.5}I_3$ perovskite solar cell precursor, the solution consisted of 258 mg H-FAI (pure hydrogenated FAI, Greatcell, Australia), 461 mg PbI_2 (anhydrous, Sigma-Aldrich, USA), 130 mg CsI (anhydrous, Sigma-Aldrich, USA), 16 mg SnF_2 (Sigma-Aldrich, USA), and 338.7 mg SnI_2 (anhydrous, bead, Sigma-Aldrich, USA) in 800 mL DMF (anhydrous, Sigma-Aldrich, USA) and 200 mL DMSO (anhydrous, Sigma-Aldrich). To prepare the corresponding D-based Pb-Sn mixed narrow-bandgap $Cs_{0.25}FA_{0.75}Sn_{0.5}Pb_{0.5}I_3$ perovskites, we used 264 mg D-FAI instead of 258 mg H-FAI, and 264 mg D-MA instead of 258 mg H-MA. Similar method was used to prepare the D-based $Cs_{0.05}FA_{0.8}MA_{0.15}PbI_{2.55}Br_{0.45}$. In the case of D-based $Cs_{0.05}FA_{0.8}MA_{0.15}PbI_{2.55}Br_{0.45}$, equal moles of D-FAI and D-MA were used instead of H-FAI or H-MAI.

4. PSC device fabrication

For Pb-Sn mixed narrow-bandgap perovskite solar cells, the prepatterned ITO substrates were sequentially cleaned by ultrasonication in acetone and isopropanol three times. The ITO/glass substrates were then dried with an N_2 gun and were UV-ozone treated for 15 min. The Poly(3,4-ethylenedioxythiophene):polystyrene sulfonate (PEDOT:PSS) (Clevios P VP Al 4083, filtered through a 0.45-mm nylon filter) were spin-coated onto ITO substrates at 3,000 rpm for 30 s and annealed on a hot plate at 150℃ for 30 min in air. After that, the substrates were transferred to a nitrogen glovebox (O_2 level < 1 ppm, H_2O < 1 ppm) to prepare the narrow-bandgap perovskite layer. The $Cs_{0.25}FA_{0.75}Sn_{0.5}Pb_{0.5}I_3$ perovskite films were deposited by spin-coating the solution as described above at 5,000 rpm for 40 s. An N_2 stream was blown over the spinning substrate for 20 s during the spinning procedure to assist with the formation of the perovskite film. Films were then annealed at 120℃ for 10 min. Finally, C60 (30 nm)/BCP (6 nm)/Ag (100 nm) were sequentially deposited by a thermal evaporator to complete the perovskite solar cells.

For $Cs_{0.05}FA_{0.8}MA_{0.15}PbI_{2.55}Br_{0.45}$ perovskite solar cells, the prepatterned ITO substrates (15 Ω sq-1) were sequentially ultrasonic cleaned using acetone and 2-propanol. The ITO substrates were then transferred into the nitrogen-filled glovebox. Then, 2 mg/ml poly (triaryl amine) (PTAA) solution was spin-coated onto the ITO substrates at 5,000 rpm for 30 s and annealed at 100°C for 10 min. The $Cs_{0.05}FA_{0.8}MA_{0.15}PbI_{2.55}Br_{0.45}$ perovskite precursor was spin-coated onto the PTAA/ITO substrate at 5,000 rpm for 30 s. After 10 s of spin-coating, 350 μL diethyl ether (DEE) was dropped onto the substrate. The resulting perovskite films were then annealed at 100°C for 10 min. After the deposition of the perovskite film, C60 (30 nm)/BCP (6 nm)/Ag (100 nm) were sequentially deposited by thermal evaporation.

5. Characterization

Devices were tested using a Newport Oriel Sol 3A solar simulator with a xenon lamp in a nitrogen-filled glovebox. The intensity of the solar simulator was calibrated to 100 mW/cm^2 AM 1.5G. The light current density-voltage (J-V) characteristic was taken with a step size of 10–30 mV and a step delay of 10 ms, unless otherwise stated. The device area was 0.1 cm^2, and the device was masked with a metal aperture to define an active area of 0.058 cm^2.

6. Computational Method

(1) Cluster calculations

Electronic structure calculations based on density functional theory (DFT) were performed with the B3LYP functional form[39,40] together with the 6-311+G(3df,2p) basis sets using the program package Gaussian 09.[41] Contributions from vdW dispersion forces were included in the form of the Grimme-D2 terms in the calculations.[42] The geometry optimization was done without applying any constraints. The convergence criteria for maximum force, RMS force, maximum displacement, and RMS displacement were set as 0.023 eV/Å, 0.015 eV/Å, 9.5×10^{-4} Å, and 6.4×10^{-4} Å, respectively. Vibrational frequencies were scaled by a factor of 0.9670.[43]

The electronic binding energy, E_b, of the H_2O molecule with an FA ionic compound is computed as:

$$E_b = (E_{FA} + E_{H2O}) - E_{FA\text{-}H2O} \quad (1)$$

where $E_{FA\text{-}H2O}$, E_{FA}, and E_{H2O} are the total energies of the FA···H_2O complex, the FA ionic compound, and the H_2O molecule, respectively. The more positive the value of E_b, the stronger the interaction.

(2) Periodic (bulk and surface) calculations

We also carried out $FASn_{0.5}Pb_{0.5}I_3$ bulk and surface calculations in the framework of DFT by applying periodic boundary conditions using the electronic structure code VASP.[44-47] The PBE

exchange-correlation functional[48] was adopted together with the van der Waals (vdW) interactions described via a pairwise force field using the DFT-D3 method of Grimme[49] with Becke-Johnson damping,[50] where the improved dispersion coefficients C_{6ij} are local geometry dependent. The projector augmented wave (PAW) method and plane wave basis sets were used with energy cutoffs of 520 eV for full-cell geometry optimization and 400 eV for geometry optimization with fixed cell parameters. The total energy was converged to 10^{-5} eV for each electronic step, and the force on each atom was converged below 0.03 eV/Å.

The $FASn_{0.5}Pb_{0.5}I_3$ (001) surface was adopted to investigate the defect formation energies of Sn^{2+} vacancies V_{Sn}^{2-}. A six-bilayer 2×2 slab was constructed with a thickness of ~35 Å and a vacuum of 15 Å to ensure negligible interaction of the slab with its neighboring images. The internal coordinates of atoms were optimized while keeping the bottom two layers fixed to the bulk positions. The Brillouin zone was sampled using a 3×3×1 Monkhorst-Pack grid for integration in the reciprocal space for the pristine and defective systems. Note that for the system with V_{Sn}^{2-}, two excess electrons were introduced into the supercell and charge was balanced by an uniform positive background.

The formation free energy of V_{Sn}^{2-} can be calculated as

$$\Delta G_f = \mu(\text{defect}) + \mu(\text{Sn}) - \mu(\text{pristine}) - 2\mu(\text{e}^-) \quad (2)$$

where μ(defect) and μ(pristine) are the Gibbs free energies of defective and pristine $FASn_{0.5}Pb_{0.5}I_3$ (001) surfaces, respectively. These values are obtained by the computed electronic total energy E and the free energy correction ΔG_{corr}, based on the frequency calculations.

$$\mu(\text{defect}) = E(\text{defect}) + \Delta G_{corr}(\text{defect}) \quad (3)$$

$$\mu(\text{pristine}) = E(\text{pristine}) + \Delta G_{corr}(\text{pristine}) \quad (4)$$

Here, μ(Sn) is the chemical potential of Sn, which is chosen to vary from the cohesive energy per atom of the Sn bulk to the chemical potential of Sn in the SnO_2 bulk, and $\mu(e^-)$ is the energy of an electron, which is set to the Fermi energy of the pristine surface.

(3) Additional computational details and results

For better comparison with the experimental results (H-based and D-based $Cs_{0.25}FA_{0.75}Sn_{0.5}Pb_{0.5}I_3$), we chose a model system, $FASn_{0.5}Pb_{0.5}I_3$, that captures the major characteristics of composition and structure and also makes the computational task affordable. The $FASn_{0.5}Pb_{0.5}I_3$ crystal is based on the crystalline structures of $FAPbI_3$,[51] with half of the Pb ions replaced by Sn. The trigonal planar FA cations $[HC(NH_2)_2]^+$ are set to lie in the central mirror plane of the unit cell with the C-H bond pointing into a cube face, whereas the $-NH_2$ groups form a hydrogen bond with the I atoms. The preference of Sn ordering at the B-site is investigated by constructing a 2×2×2 supercell and sampling three different Sn ordering orientations along the three principal vectors in the perovskite conventional cell (**Fig. S11**). The total electronic energy only differs on the order of 0.0002 eV per formula unit ($FASn_{0.5}Pb_{0.5}I_3$), suggesting that it is not sensitive to the ordering of substitution of Sn in the bulk. We chose the lowest energy configuration for the surface calculations.

Energetics were considered for four surface terminations: (001) surface with FAI termination, (001) surface with PbI_2 termination, $(00\bar{1})$ surface with FAI termination, and $(00\bar{1})$ surface with PbI_2 termination (see **Fig. S12**). The (001) surface has the $-NH_2$ group (negatively charged) pointing toward the surface, whereas the −CH group (positively charged) points away from the surface. Thus, the intrinsic dipole moment of the FA ion points from the surface to the bulk region for the (001) surface, and in the opposite direction for the $(00\bar{1})$ surface. The calculated total energy shows that the (001) surface with FAI termination has the lowest energy. Therefore, we chose it for the calculation of formation energies of Sn vacancies.

The Sn vacancy is formed by removing an Sn atom from the pristine surface. The Sn vacancy can carry different charge states—0, -1, and -2—with the -2 charge state (V_{Sn}^{2-}) being the lowest in formation energy (*30*). To study the dependence of the vacancy formation energy on the location of the vacancy underneath the surface, we generated the Sn vacancy in the first, second, and third layers of the (001) surface. It is interesting to note that the orientation of FA cations tilted near the Sn vacancy. To reveal the deuteration effect by substituting D for H in the FA molecule, we calculated the vibrational frequencies of the system, thereby obtaining the free energy corrections (at $T = 298.15$ K) to the formation energy of V_{Sn}^{2-} (see **Table S3**). The positions of the Pb, Sn, and I atoms are constrained in these frequency calculations.

References

1. L. Wang, H. Zhou, J. Hu, B. Huang, M. Sun, B. Dong, G. Zheng, Y. Huang, Y. Chen, L. Li, Z. Xu, N. Li, Z. Liu, Q. Chen, L.-D. Sun, C.-H. Yan, A Eu^{3+}-Eu^{2+} ion redox shuttle imparts operational durability to Pb-I perovskite solar cells. *Science* **363**, 265-270 (2019).

2. R. Azmi, E. Ugur, A. Seitkhan, F. Aljamaan, A. S. Subbiah, J. Liu, G. T. Harrison, M. I. Nugraha, M. K. Eswaran, M. Babics, Y. Chen, F. Xu, T. G. Allen, A. u. Rehman, C.-L. Wang, T. D. Anthopoulos, U. Schwingenschlögl, M. D. Bastiani, E. Aydin, S. D. Wolf, Damp heat-stable perovskite solar cells with tailored-dimensionality 2D/3D heterojunctions. *Science* **376**, 73-77 (2022).

3. M. V. Khenkin, E. A. Katz, A. Abate, G. Bardizza, J. J. Berry, C. Brabec, F. Brunetti, V. Bulović, Q. Burlingame, A. Di Carlo, R. Cheacharoen, Y.-B. Cheng, A. Colsmann, S. Cros, K. Domanski, M. Dusza, C. J. Fell, S. R. Forrest, Y. Galagan, D. Di Girolamo, M. Grätzel, A. Hagfeldt, E. von Hauff, H. Hoppe, J. Kettle, H. Köbler, M. S. Leite, S. Liu, Y.-L. Loo, J. M. Luther, C.-Q. Ma, M. Madsen, M. Manceau, M. Matheron, M. McGehee, R. Meitzner, M. K. Nazeeruddin, A. F. Nogueira, Ç. Odabaşı, A. Osherov, N.-G. Park, M. O. Reese, F. De Rossi, M. Saliba, U. S. Schubert, H. J. Snaith, S. D. Stranks, W. Tress, P. A. Troshin, V. Turkovic, S. Veenstra, I. Visoly-Fisher, A. Walsh, T. Watson, H. Xie, R. Yıldırım, S. M. Zakeeruddin, K. Zhu, M. Lira-Cantu, Consensus statement for stability assessment and reporting for perovskite photovoltaics based on ISOS procedures. *Nature Energy* **5**, 35-49 (2020).

4. V. C. A. Taylor, D. Tiwari, M. Duchi, P. M. Donaldson, I. P. Clark, D. J. Fermin, T. A. A. Oliver, Investigating the Role of the Organic Cation in Formamidinium Lead Iodide Perovskite Using Ultrafast Spectroscopy. *The journal of physical chemistry letters* **9**, 895-901 (2018).

5. A. A. Bakulin, O. Selig, H. J. Bakker, Y. L. A. Rezus, C. Müller, T. Glaser, R. Lovrincic, Z. Sun, Z. Chen, A. Walsh, J. M. Frost, T. L. C. Jansen, Real-Time Observation of Organic Cation Reorientation in Methylammonium Lead Iodide Perovskites. *The journal of physical chemistry letters* **6**, 3663-3669 (2015).

6. J. M. Frost, K. T. Butler, F. Brivio, C. H. Hendon, M. van Schilfgaarde, A. Walsh, Atomistic Origins of High-Performance in Hybrid Halide Perovskite Solar Cells. *Nano Letters* **14**, 2584-2590 (2014).

7. Y. Fu, M. P. Hautzinger, Z. Luo, F. Wang, D. Pan, M. M. Aristov, I. A. Guzei, A. Pan, X. Zhu, S. Jin, Incorporating Large A Cations into Lead Iodide Perovskite Cages: Relaxed Goldschmidt Tolerance Factor and Impact on Exciton–Phonon Interaction. *ACS Central Science* **5**, 1377-1386 (2019).

8. G. Abdelmageed, C. Mackeen, K. Hellier, L. Jewell, L. Seymour, M. Tingwald, F. Bridges, J. Z. Zhang, S. Carter, Effect of temperature on light induced degradation in

methylammonium lead iodide perovskite thin films and solar cells. *Solar Energy Materials and Solar Cells* **174**, 566-571 (2018).

9. X. Dong, X. Fang, M. Lv, B. Lin, S. Zhang, J. Ding, N. Yuan, Improvement of the humidity stability of organic–inorganic perovskite solar cells using ultrathin Al2O3 layers prepared by atomic layer deposition. *Journal of Materials Chemistry A* **3**, 5360-5367 (2015).

10. N. H. Nickel, F. Lang, V. V. Brus, O. Shargaieva, J. Rappich, Unraveling the Light-Induced Degradation Mechanisms of CH3NH3PbI3 Perovskite Films. *Advanced Electronic Materials* **3**, 1700158 (2017).

11. R. Wang, M. Mujahid, Y. Duan, Z.-K. Wang, J. Xue, Y. Yang, A Review of Perovskites Solar Cell Stability. *Advanced Functional Materials* **29**, 1808843 (2019).

12. C. C. Boyd, R. Cheacharoen, T. Leijtens, M. D. McGehee, Understanding Degradation Mechanisms and Improving Stability of Perovskite Photovoltaics. *Chemical Reviews* **119**, 3418-3451 (2019).

13. K. L. Svane, A. C. Forse, C. P. Grey, G. Kieslich, A. K. Cheetham, A. Walsh, K. T. Butler, How Strong Is the Hydrogen Bond in Hybrid Perovskites? *The journal of physical chemistry letters* **8**, 6154-6159 (2017).

14. Z. Fan, H. Xiao, Y. Wang, Z. Zhao, Z. Lin, H.-C. Cheng, S.-J. Lee, G. Wang, Z. Feng, W. A. Goddard, Y. Huang, X. Duan, Layer-by-Layer Degradation of Methylammonium Lead Tri-iodide Perovskite Microplates. *Joule* **1**, 548-562 (2017).

15. T. D. Siegler, W. A. Dunlap-Shohl, Y. Meng, Y. Yang, W. F. Kau, P. P. Sunkari, C. E. Tsai, Z. J. Armstrong, Y.-C. Chen, D. A. C. Beck, M. Meilă, H. W. Hillhouse, Water-Accelerated Photooxidation of CH3NH3PbI3 Perovskite. *Journal of the American Chemical Society* **144**, 5552-5561 (2022).

16. Y. Ouyang, Y. Li, P. Zhu, Q. Li, Y. Gao, J. Tong, L. Shi, Q. Zhou, C. Ling, Q. Chen, Z. Deng, H. Tan, W. Deng, J. Wang, Photo-oxidative degradation of methylammonium lead iodide perovskite: mechanism and protection. *Journal of Materials Chemistry A* **7**, 2275-2282 (2019).

17. J. Wei, Q. Wang, J. Huo, F. Gao, Z. Gan, Q. Zhao, H. Li, Mechanisms and Suppression of Photoinduced Degradation in Perovskite Solar Cells. *Advanced Energy Materials* **11**, 2002326 (2021).

18. N. Aristidou, C. Eames, I. Sanchez-Molina, X. Bu, J. Kosco, M. S. Islam, S. A. Haque, Fast oxygen diffusion and iodide defects mediate oxygen-induced degradation of perovskite solar cells. *Nature Communications* **8**, 15218 (2017).

19. S. Wang, Y. Jiang, Emilio J. Juarez-Perez, Luis K. Ono, Y. Qi, Accelerated degradation of methylammonium lead iodide perovskites induced by exposure to iodine vapour. *Nature Energy* **2**, 16195 (2016).

20. G. Niu, W. Li, F. Meng, L. Wang, H. Dong, Y. Qiu, Study on the stability of CH3NH3PbI3 films and the effect of post-modification by aluminum oxide in all-solid-state hybrid solar cells. *Journal of Materials Chemistry A* **2**, 705-710 (2014).

21. P. Chen, W.-J. Ong, Z. Shi, X. Zhao, N. Li, Pb-Based Halide Perovskites: Recent Advances in Photo(electro)catalytic Applications and Looking Beyond. *Adv. Funct. Mater.* **30**, 1909667 (2020).

22 Tong, J.; Song, Z.; Kim, D. H.; Chen, X.; Chen, C.; Palmstrom, A. F.; Ndione, P. F.; Reese, M. O.; Dunfield, S. P.; Reid, O. G.; Liu, J.; Zhang, F.; Harvey, S. P.; Li, Z.; Christensen, S. T.; Teeter, G.; Zhao, D.; Al-Jassim, M. M.; van Hest, M. F. A. M.; Beard, M. C.; Shaheen, S. E.; Berry, J. J.; Yan, Y.; Zhu, K. Carrier Lifetimes of >1 μs in Sn-Pb perovskites Enable Efficient all-Perovskite Tandem Solar Cells. *Science 364*, 475– 479 (2019).

23. M. Zhang, Z. Zhang, H. Cao, T. Zhang, H. Yu, J. Du, Y. Shen, X.-L. Zhang, J. Zhu, P. Chen, M. Wang, Recent progress in inorganic tin perovskite solar cells. *Materials Today Energy* **23**, 100891 (2022).

24. T. Leijtens, R. Prasanna, A. Gold-Parker, M. F. Toney, M. D. McGehee, Mechanism of Tin Oxidation and Stabilization by Lead Substitution in Tin Halide Perovskites. *ACS Energy Letters* **2**, 2159-2165 (2017).

25. L. Lanzetta, T. Webb, N. Zibouche, X. Liang, D. Ding, G. Min, R. J. E. Westbrook, B. Gaggio, T. J. Macdonald, M. S. Islam, S. A. Haque, Degradation mechanism of hybrid tin-based perovskite solar cells and the critical role of tin (IV) iodide. *Nature Communications* **12**, 2853 (2021).

26. F. Wang, J. Ma, F. Xie, L. Li, J. Chen, J. Fan, N. Zhao, Organic Cation-Dependent Degradation Mechanism of Organotin Halide Perovskites. *Adv. Funct. Mater.* **26**, 3417-3423 (2016).

27. J. J. Katz, Chemical and biological studies with deuterium. *American Scientist* **48**, 544-580 (1960).

28. S. Scheiner, M. Čuma, Relative Stability of Hydrogen and Deuterium Bonds. *Journal of the American Chemical Society* **118**, 1511-1521 (1996).

29. Z. Li, J. Ji, C. Zhang, Q. Hou, P. Jin, First-Principles Study on the Oxygen–Light-Induced Iodide Vacancy Formation in FASnI3 Perovskite. *The Journal of Physical Chemistry C* **124**, 14147-14157 (2020).

30. E. H. Kim, J. H. Lee, S. H. Kim, J. H. Gu, D. Lee, A-Site Effect on the Oxidation Process of Sn-Halide Perovskite: First-Principles Calculations. *The Journal of Physical Chemistry Letters* **12**, 9691-9696 (2021).

31. J. W. Heinecke, F. F. Hsu, J. R. Crowley, S. L. Hazen, C. Leeuwenburgh, D. M. Mueller, J. E. Rasmussen, J. Turk, in *Methods in Enzymology*. (Academic Press, 1999), vol. 300, pp. 124-144.

32. S. S. Iyer, Z.-P. Zhang, G. E. Kellogg, H. T. Karnes, Evaluation of Deuterium Isotope Effects in Normal-Phase LC-MS-MS Separations Using a Molecular Modeling Approach. *Journal of Chromatographic Science* **42**, 383-387 (2004).

33. E. A. Halevi, Polarity differences between deuterated and normal molecules. *Transactions of the Faraday Society* **54**, 1441-1446 (1958).

34. E. A. Halevi, E. N. Haran, B. Ravid, Dipole moment and polarizability differences between NH3 and ND3. *Chemical Physics Letters* **1**, 475-476 (1967).

35. C. Kampmeyer, J.V. Johansen, C. Holmberg, M. Karlson, S. K. Gersing, H. N. Bordallo, B. B. Kragelund, M. H. Lerche, I. Jourdain, J. R. Winther, R. Hartmann-Petersen, Mutations in a Single Signaling Pathway Allow Cell Growth in Heavy Water. *ACS Synthetic Biology* 9, 733-748 (2020).

36. R. A. Kerner, T. H. Schloemer, P. Schulz, J. J. Berry, J. Schwartz, A. Sellinger, B. P. Rand, Amine additive reactions induced by the soft Lewis acidity of Pb^{2+} in halide perovskites. Part I: evidence for Pb–alkylamide formation. *Journal of Materials Chemistry C* **7**, 5251-5259 (2019).

37. J. P. Reid, R. A. Loomis, S. R. Leone, Competition between N−H and N−D Bond Cleavage in the Photodissociation of NH_2D and ND_2H. *The Journal of Physical Chemistry A* **104**, 10139-10149 (2000).

38. Gong, J.; Yang, M.; Ma, X.; Schaller, R. D.; Liu, G.; Kong, L.; Yang, Y.; Beard, M. C.; Lesslie, M.; Dai, Y.; Huang, B.; Zhu, K.; Xu, T. Electron–Rotor Interaction in Organic–Inorganic Lead Iodide Perovskites Discovered by Isotope Effect, *J. Phys. Chem. Lett. 7*, 2879–2887(2016).

39. C. Lee, W. Yang, R. G. Parr, Development of the Colle-Salvetti correlation-energy formula into a functional of the electron density. *Physical Review B* **37**, 785-789 (1988).

40. A. D. Becke, Density-functional thermochemistry. III. The role of exact exchange. *The Journal of Chemical Physics* **98**, 5648-5652 (1993).

41. M. J. Frisch, G. W. Trucks, H. B. Schlegel, G. E. Scuseria, M. A. Robb, J. R. Cheeseman, G. Scalmani, V. Barone, G. A. Petersson, H. Nakatsuji, X. Li, M. Caricato, A. Marenich, J. Bloino, B. G. Janesko, R. Gomperts, B. Mennucci, H. P. Hratchian, J. V. Ortiz, A. F.

Izmaylov, J. L. Sonnenberg, D. Williams-Young, F. Ding, F. Lipparini, F. Egidi, J. Goings, B. Peng, A. Petrone, T. Henderson, D. Ranasinghe, V. G. Zakrzewski, J. Gao, N. Rega, G. Zheng, W. Liang, M. Hada, M. Ehara, K. Toyota, R. Fukuda, J. Hasegawa, M. Ishida, T. Nakajima, Y. Honda, O. Kitao, H. Nakai, T. Vreven, K. Throssell, J. A. Montgomery, J. E. P. Jr., F. Ogliaro, M. Bearpark, J. J. Heyd, E. Brothers, K. N. Kudin, V. N. Staroverov, T. Keith, R. Kobayashi, J. Normand, K. Raghavachari, A. Rendell, J. C. Burant, S. S. Iyengar, J. Tomasi, M. Cossi, J. M. Millam, M. Klene, C. Adamo, R. Cammi, J. W. Ochterski, R. L. Martin, K. Morokuma, O. Farkas, J. B. Foresman, D. J. Fox, Gaussian09, revision D.01; Gaussian, Inc.: Wallingford, CT. (2009).

42. S. Grimme, Semiempirical GGA-type density functional constructed with a long-range dispersion correction. *Journal of Computational Chemistry* **27**, 1787-1799 (2006).

43. K. K. Irikura, R. D. Johnson, R. N. Kacker, Uncertainties in Scaling Factors for ab Initio Vibrational Frequencies. *The Journal of Physical Chemistry A* **109**, 8430-8437 (2005).

44. G. Kresse, J. Hafner, Ab initio molecular dynamics for liquid metals. *Physical Review B* **47**, 558-561 (1993).

45. G. Kresse, J. Hafner, Ab initio molecular-dynamics simulation of the liquid-metal--amorphous-semiconductor transition in germanium. *Physical Review B* **49**, 14251-14269 (1994).

46. G. Kresse, J. Furthmüller, Efficiency of ab-initio total energy calculations for metals and semiconductors using a plane-wave basis set. *Computational Materials Science* **6**, 15-50 (1996).

47. G. Kresse, J. Furthmuller, Efficient iterative schemes for ab initio total-energy calculations using a plane-wave basis set. *Physical Review B* **54**, 11169-11186 (1996).

48. J. P. Perdew, K. Burke, M. Ernzerhof, Generalized gradient approximation made simple. *Physical Review Letters* **77**, 3865-3868 (1996).

49. S. Grimme, J. Antony, S. Ehrlich, H. Krieg, A consistent and accurate ab initio parametrization of density functional dispersion correction (DFT-D) for the 94 elements H-Pu. *The Journal of Chemical Physics* **132**, 154104 (2010).

50. S. Grimme, S. Ehrlich, L. Goerigk, Effect of the damping function in dispersion corrected density functional theory. *Journal of Computational Chemistry* **32**, 1456-1465 (2011).

51. M. T. Weller, O. J. Weber, J. M. Frost, A. Walsh, Cubic Perovskite Structure of Black Formamidinium Lead Iodide, α-[HC(NH2)2]PbI3, at 298 K. *The Journal of Physical Chemistry Letters* **6**, 3209-3212 (2015).

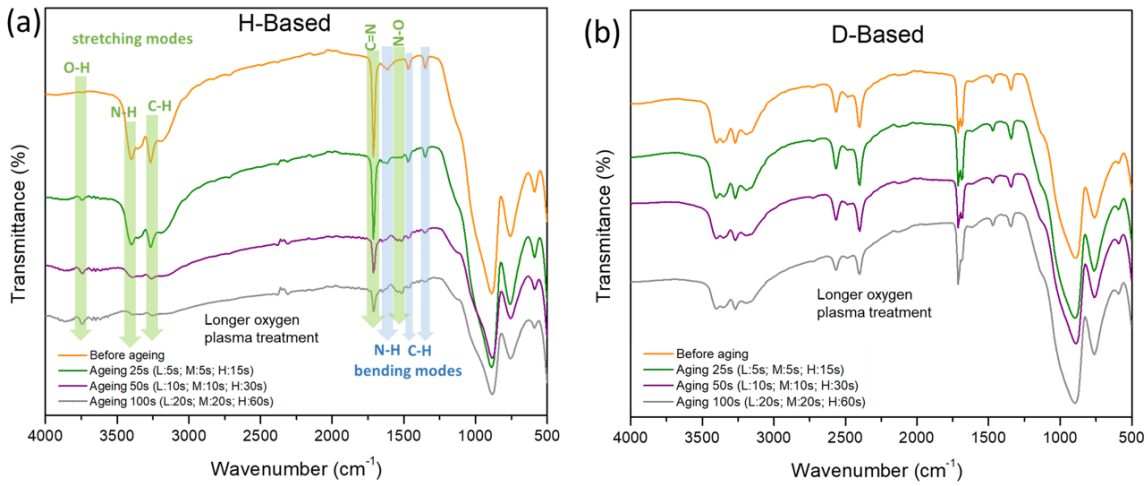

Figure 1. (**a**) FTIR of H-based perovskite films (composition: $(H\text{-}FASnI_3)_{0.6}(H\text{-}MAPbI_3)_{0.4}$) before and after oxygen plasma treatment for different aging durations. Three levels of oxygen plasma intensity were used (L = low energy; M = medium energy; H = high energy). (**b**) FTIR of D-based perovskite films (composition: $(D\text{-}FASnI_3)_{0.6}(D\text{-}MAPbI_3)_{0.4}$) before and after oxygen plasma treatment using the same aging conditions as in the H-based perovskite film.

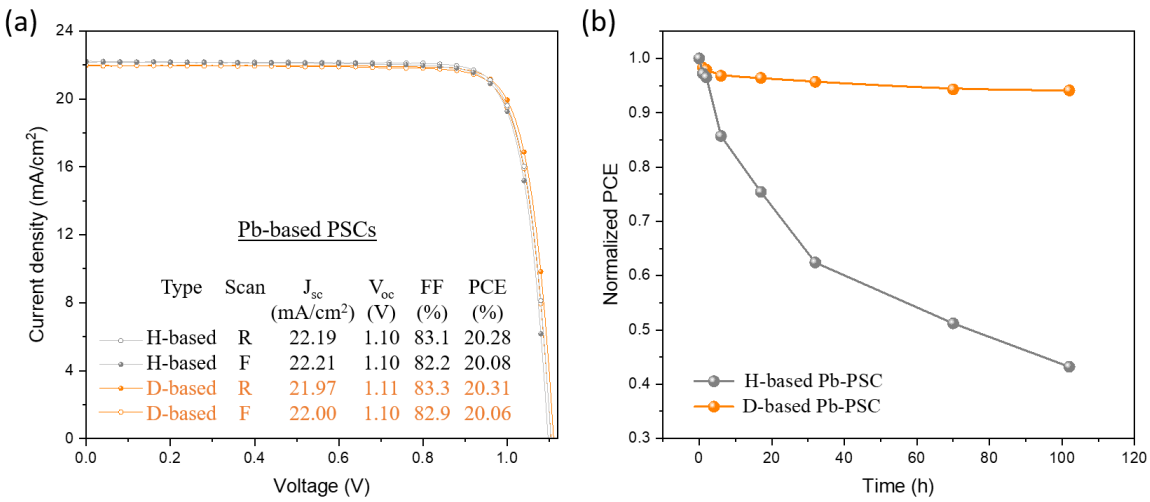

Figure 2. (a) J-V characteristics with reverse (R) and forward (F) scans for H-based and D-based $Cs_{0.05}MA_{0.15}FA_{0.8}PbI_{2.55}Br_{0.45}$ PSCs; **(b)** thermal stability evaluation of the corresponding unencapsulated devices at 85ºC in dry air.

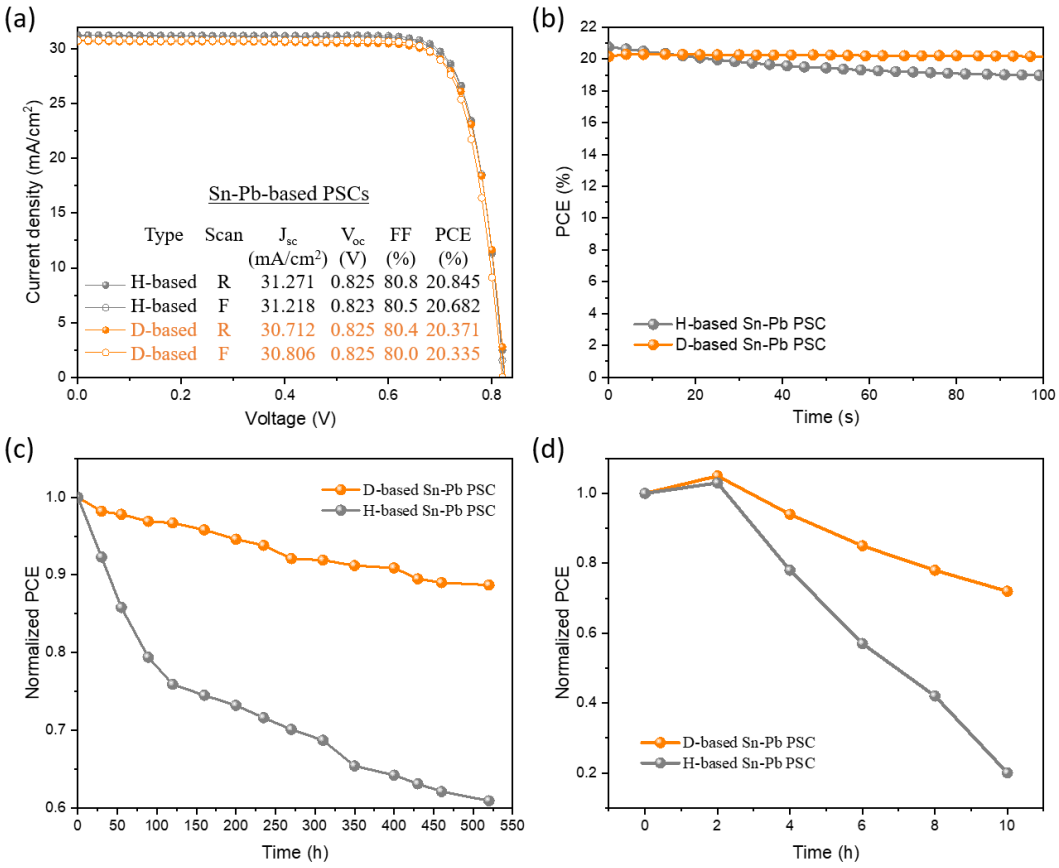

Figure 3. PV performance comparison of H-FAI- and D-FAI-based $Cs_{0.25}FA_{0.75}Sn_{0.5}Pb_{0.5}I_3$ narrow-bandgap PSCs (all unencapsulated). (**a**) Comparison of J-V curves. (**b**) Comparison of stabilized power output. (**c**) Comparison of operational stability at RH = ~50% and temperature of ~50°C under continuous light illumination in air. (**d**) Comparison of ambient stability of the Pd-Sn narrow bandgaps PCSs under 82% RH. Devices were not encapsulated.

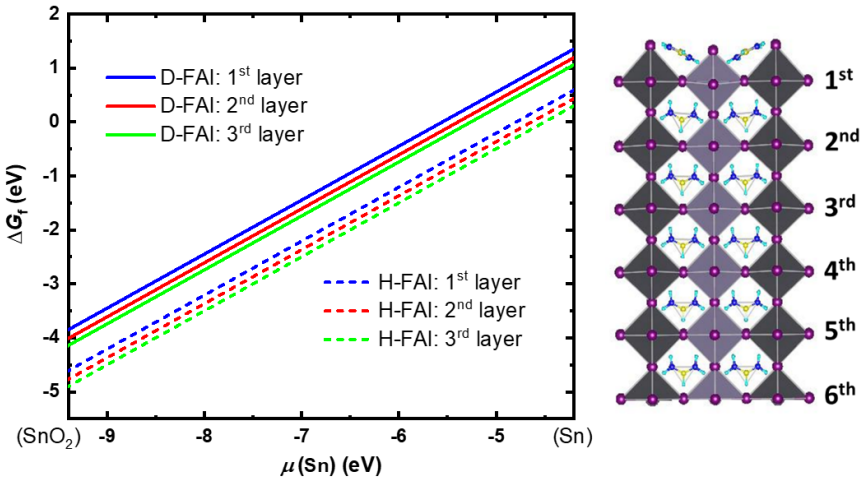

Figure 4. Sn^{2+} vacancy (V_{Sn}^{2-}) formation free energies as a function of the Sn chemical potential μ(Sn) for vacancies located at different layers beneath the top surface layer of a model system of the $FASn_{0.5}Pb_{0.5}I_3$ (001) surface. Symbols for atoms: C in yellow, N in navy blue, H in light blue, I in purple, Pb in gray, and Sn in light pink.

Acknowledgments

T.X. acknowledges the support from the National Science Foundation (DMR 1806152). The work at the National Renewable Energy Laboratory was supported by the U.S. Department of Energy under Contract No. DE-AC36-08GO28308 with Alliance for Sustainable Energy, Limited Liability Company (LLC), the Manager and Operator of the National Renewable Energy Laboratory. K.Z. and J.T. acknowledge the support on perovskite synthesis and device fabrication and characterization from the De-Risking Halide Perovskite Solar Cells program of the National Center for Photovoltaics, funded by the U.S. Department of Energy, Office of Energy Efficiency and Renewable Energy, Solar Energy Technologies Office. The views expressed in the article do not necessarily represent the views of the DOE or the U.S. Government. The U.S. Government retains and the publisher, by accepting the article for publication, acknowledges that the U.S. Government retains a nonexclusive, paid-up, irrevocable, worldwide license to publish or reproduce the published form of this work, or allow others to do so, for U.S. Government purposes. T.X. also thanks Prof. Peijun Guo at Yale University for help with the initial optic study.

Author Contributions

T.X. and K.Z. designed and supervised the research. J.T. fabricated and characterized perovskite thin films and devices. X.L. and J.W. prepared the deterium-based precursory materials and evaluated the antioxidation properties of the perovskite thin films. H.H. conducted the theoretical calculation and simulation. All authors discussed the results and contributed to manuscript preparation.

Competing Interests

The authors declare no competing interests.

Data and Materials Availability

The data, codes, associated protols and materials etc. that support the findings of this study are available from the corresponding authors upon reasonable request.

803